INTEGRATION OF ATTITUDE CHARACTERIZATION IN A SPACE DEBRIS CATALOGUE USING LIGHT CURVES

D. Vallverdú Cabrera[(1)], J. Utzmann[(1)], and R. Förstner[(2)]

[(1)]*Airbus DS, 88039 Friedrichshafen, Germany, Email: {david.vallverdu_cabrera, jens.utzmann}@airbus.com*
[(2)]*Universität der Bundeswehr München, 85579 Neubiberg, Germany, Email: roger.foerstner@uinbw.de*

ABSTRACT

The Security in Space team of Airbus Defence and Space Germany develops the Special Perturbations Orbit determination and Orbit analysis toolKit (SPOOK), a software framework aimed at maintaining a catalogue of space objects with information on their orbital ephemeris. SPOOK can perform all the main activities of the Space Surveillance and Tracking (SST) workflow, including observation planning, optical and radar measurement simulation or processing of real world data, either from the in-house Airbus Robotic Telescope (ART) or from third parties, tracklet linking, tracklet correlation and orbit determination. With the aim to include further object characteristics into the catalogue, this paper describes how this workflow is updated to add systematic object characterization capabilities in SPOOK. In particular, this paper focuses on attitude characterization using light curves. To achieve this goal, two main new blocks have been added to SPOOK: light curve simulation and shape-independent attitude characterization – i.e., the shape of the object is not taken into account to estimate its attitude state.

Keywords: Light curve; attitude determination; object characterization; SPOOK.

1. INTRODUCTION

Not only is the space environment near the Earth more populated than ever [9], but also the space debris population is expected to increase dramatically unless considerable mitigation becomes possible [31]. Object characterization, among the typical Space Surveillance and Tracking (SST) activities, is paramount to enable mitigation processes such as Active Debris Removal (ADR). E.g., the shape and attitude of a space object that is to be deorbited need to be known so that a successful ADR mission can planned.

Light curves – series of brightness measurements, closely spaced in time, taken from a single object with an optical telescope – encode the object characteristics of attitude, shape, size and reflective properties of the surface. Thus, they are one of the main resources available to perform characterization of objects for which resolved imagery is not possible – which is the case for most space debris objects. Characterization of non-collaborative space objects has been explored for decades in the asteroid community [15, 16, 27]. To the present day, many techniques therein have been transferred and adapted to the characterization of man-made objects, and new ones have been developed [8, 11, 14, 18, 21, 34].

This paper presents the integration of shape-independent attitude determination techniques that use light curves as measurements into the Special Perturbations Orbit determination and Orbit analysis toolKit (SPOOK), a software framework developed at Airbus DS which can perform multiple SSA-related tasks [20, 23]. The paper is structured as follows: first, after a brief summary of the capabilities of SPOOK previous to this work (Section 2), the new capabilities of SPOOK are presented: light curve simulation (Section 3), obtention of light curves from real images (Section 4), light curve preprocessing (Section 5) and attitude characterization (Section 6). The paper concludes by discussing the results of the attitude determination pipeline of SPOOK on real and simulated examples (Section 7).

2. BACKGROUND

SPOOK is a software framework with several distinct capabilities within the scope of SST and SSA. The main capabilities are [20, 23, 24]:

- End to end pipeline to create and maintain a catalogue with the orbital ephemeris of space objects, using radar and optical measurements;
- Simulation of radar and optical measurements of objects with simple shape (homogeneous sphere or randomly tumbling plate);
- Observation planning tools to program an optical telescope;
- Sensor astrometric calibration based on the well known ephemeris of specific objects;

- Probabilistic conjunction assessment.

Furthermore, Airbus DS owns and operates the Airbus Robotic Telescope (ART), located in Extremadura, Spain, with 40 cm of aperture and a rectangular field of view of $2.15^{\text{o}} \times 1.43^{\text{o}}$ [28].

3. LIGHT CURVE SIMULATION

SPOOK has sensor simulation capabilities that can be used to produce synthetic astrometric measurements [23]. The present work has extended the benefits of this capability to the photometric type of measurements by adding light curve simulating functionality into SPOOK.

To predict the measured light intensity reflected by a target object, which is then measured from an arbitrary observer telescope, the first addition to SPOOK deals with the modelling of 3D objects as polyhedrons represented by their outer surface, which in turn is divided into triangular facets. Each facet has its own reflective properties, represented by a parametrized Bidirectional Reflectance Distribution Function (BRDF). The second addition focuses on solving the shadowing problem, which, in short, determines the contribution of each facet to total reflection, constrained by the shadowing that other facets of the object may inflict upon itself. Finally, SPOOK has been further extended with attitude modelling and propagation, in addition to the orbital position and velocity. The rest of this section describes how these problems have been approached.

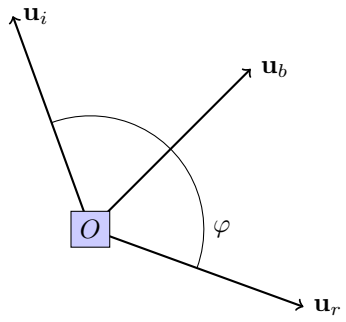

Figure 1. Observation geometry projected on the plane formed by the Sun, the object and the observer.

These three additions enable the simulation of the the complete observation geometry, shown in Figure 1 projected on the plane formed by the Sun, the object (O) and the observer. The vectors are all unitary: $\mathbf{u}_i$ is the incident direction, toward the Sun; $\mathbf{u}_r$, the reflected direction, toward the observer; and $\mathbf{u}_b$ is the bisector of the other two, a.k.a. Phase Angle Bisector or PAB; The angle between $\mathbf{u}_i$ and $\mathbf{u}_r$ is known as the phase angle, $\varphi = \angle(\mathbf{u}_i, \mathbf{u}_r)$.

3.1. 3D Object Reflectance

Three dimensional objects are modelled within SPOOK as an euclidean region bound by a closed set of triangular surfaces, called facets. This is, an object O is delimited by N_f facets with three vertices each, connected with each other along their edges. A Bidirectional Reflectance Distribution Function (BRDF) as defined by [19],

$$f_r(\lambda, \mathbf{u}_i, \mathbf{u}_r) = \frac{dL_{r,\lambda}(\lambda, \mathbf{u}_r)}{dE_{i,\lambda}(\lambda, \mathbf{u}_i)}\,, \tag{1}$$

captures the reflective properties of the different facets of the object. The BRDF represented by f_r gives the ratio, in inverse steradians or sr^{-1}, between the reflected spectral[1] radiance $dL_{r,\lambda}$ that leaves a surface element in the direction $\mathbf{u}_r$, in $\text{Wsr}^{-1}\text{m}^{-3}$, over the spectral irradiance $dE_{i,\lambda}$ incident on the surface element in the direction opposite to $\mathbf{u}_i$, in Wm^{-3}. The differential form is commonly used to allow for contributions to the total $L_{r,\lambda}$ other than $dE_{i,\lambda}$.

Figure 2 shows the same observation geometry from Figure 1, but from the point of view of a surface element of the object with anisotropic directions $\mathbf{u}_u$ and $\mathbf{u}_v$ and normal $\mathbf{n}$. The angle pairs (θ_i, ϕ_i), (θ_r, ϕ_r) and (α, β) are the (polar, azimuth) spherical coordinates, as seen by the facet coordinate system with base $[\mathbf{u}_u, \mathbf{u}_v, \mathbf{n}]$, of the incident, reflected and PAB directions respectively.

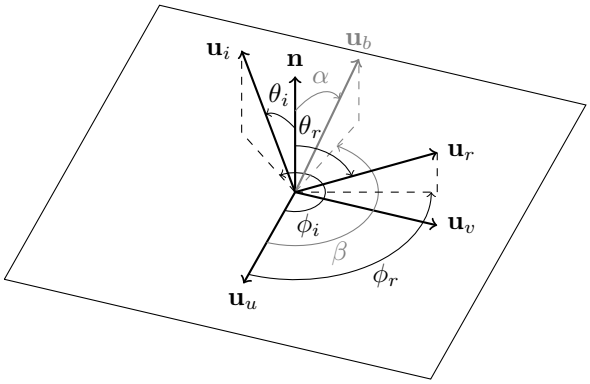

Figure 2. The observation geometry for a surface element.

Although several BRDFs exist with varying degrees of complexity, from simple Lambertian to empirical look-up tables, SPOOK implements the rather simple Cook-Torrance (CT) and Ashikhmin-Shirley (AS) models, which account for specular and diffuse reflectance and conserve energy notwithstanding. Additionally, AS can model the anisotropy of the surface. They have been chosen for their *de facto* acceptance in the literature relevant to light curve modelling [10, 33]. For further details on their implementation the reader may refer to [1, 7, 33].

[1] Hence the λ subscript indicating derivative over wavelength. From here onward, the explicit dependency on λ will be dropped from spectral quantities, as it will be implicit in the subindex – e.g. $L_{i,\lambda}(\mathbf{u_i}) \equiv L_{i,\lambda}(\lambda, \mathbf{u_i})$.

The Sun is assumed to emit black-body radiation, hence irradiance reflected by each facet is obtained by integrating its BRDF multiplied by Planck's law applied to the Sun over the wavelength bandwith of interest, B_λ. Therefore, the total irradiance E_a reflected from the object that reaches the telescope, for a given observation geometry, is computed in SPOOK from the contribution of each facet, taking self-shadowing into account (see next section). Apparent magnitude is then

$$m_A = -2.5 \log_{10} \left(\frac{E_a}{E_{a,0}} \right) , \tag{2}$$

where $E_{a,0}$ is the irradiance that would be received from the Vega star under the same observation conditions.

Finally, SPOOK can additionally obtain the measured photon flux F_a, by applying the transmissivity and quantum efficiency curves of an arbitrary telescope; and the associated signal to noise ratio (SNR), by further considering the inherent noise sources of a specific setup. The instrumental magnitude measurement is then estimated as

$$m_I = -2.5 \log_{10} F_a \, , \tag{3}$$

where F_a is commonly used as an approximation of E_a.

3.2. 3D to 0D Rendering

One of the bottlenecks of light curve modelling is the computation of the non-shadowed area $\mathcal{A}$ of each facet. In the particular case for convex objects, $\mathcal{A} = \delta(\theta_i, \theta_r)A$, where A is the area of the facet and

$$\delta(\theta_i, \theta_r) = \begin{cases} 1 & \cos\theta_i > 0 \text{ and } \cos\theta_r > 0 \, , \\ 0 & \text{otherwise} \, . \end{cases} \tag{4}$$

For non-convex objects, however, the computation of $\mathcal{A}$ complicates greatly. SPOOK deals with this via the algorithm called *shadow projection*, developed in-house. The output of this algorithm is directly the product $\mathcal{A}\cos(\theta_r)$. It works by comparing which facets are in front of each other, both from the incident and reflected directions. It then projects the covered portions of the facets, i.e. the shadows, on top of the facets themselves, hence the name of the algorithm; it then subtracts the area of the projected shadows from the original area of the corresponding facets. Shadow detection and subtraction uses the polygon boolean operations of intersection and difference, respectively, which can be performed e.g. with the algorithms from [30].

A necessary condition for the shadow projection algorithm to work is that the facets that define O can only intersect with each other at their borders – i.e. edges or vertices.

Figure 3 gives a graphical explanation of the algorithm applied to an object composed by the three facets $F^{(1)}$ (blue), $F^{(3)}$ (brown) and $F^{(3)}$ (lilac), which extend indefinitely along the direction perpendicular to the paper. These facets and their projections are represented by solid lines of the respective colour. The dashed lines are the projection planes, symbolized by U_i and U_r, with normals $\mathbf{u}_i$ and $\mathbf{u}_r$, respectively. Thick gray overlays represent shadows, and the also gray arrows *track* the shadow projection between facets and from U_i to U_r. The projections are drawn with an offset to their respective planes, to indicate the relative distance w.r.t. the illumination source or the observer, a notion that is key to decide which of the overlapping facets is shadowing the other. In this example, facet $F^{(1)}$ is illuminated and visible, but has two portions blocked, one by $F^{(2)}$ on the U_r plane, and the other by $F^{(3)}$ on the U_i plane.

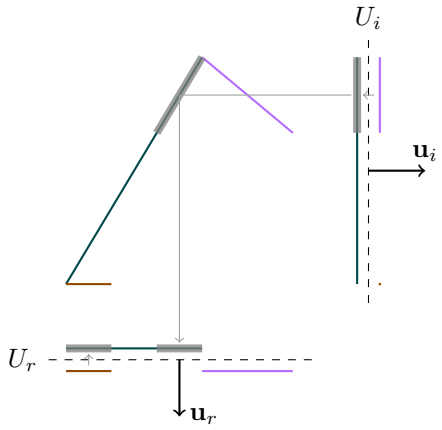

Figure 3. 2D illustration of the shadow projection algorithm.

In terms of speed, this algorithm needs to check twice (once in each projection) the intersection of the 2-combinations of the N_f set of facets. This is, it needs to perform $N_f(N_f - 1)$ polygon intersection operations plus at most this many polygon subtractions (one per non-empty intersection) and half as many $i \to r$ projections (one per non-empty intersection on U_i). Thus, for big N_f, the computation time scales with $O({N_f}^2)$. Furthermore, the most resource-consuming parts of the algorithm can be parallelized.

One final advantage of this algorithm is that areas visible from the observer point of view, regardless of the illumination condition, can be extracted without any additional computational effort. This is useful to account for radiated light, typically more significant toward infrared spectrum.

3.3. Attitude Propagation

Before this work, SPOOK could only propagate the position and velocity of a space object through time. Attitude propagation, necessary for detailed light curve simulation, has been incorporated using quaternion representation. The current implementation can only consider

torque-free attitude dynamics, by ensuring the conservation of angular momentum given the inertia tensor of the object, together with a reference attitude and angular velocity at a known instance of time. Thus, it is not yet suitable to simulate long light curves of objects subject to significant torques e.g. due to atmospheric drag.

4. LIGHT CURVES FROM IMAGES

This section discusses how light curves can be extracted from real images within the framework of SPOOK, ART and the SSA toolkit at Airbus DS by diverse means, depending on the nature of the images from which the light curves are to be obtained. In most cases, light curves are obtained from series of images taken during a tracking observation scenario. This is, the telescope pointing is fixed to the sky coordinates of an Earth-orbiting object of interest. Thus, in the images taken this way, the object itself, together with any other objects in a similar orbit, appear as a point feature, while the rest of objects in that sky region, including stars and objects in different orbits, appear as straight lines or streaks.

Two different methods to extract light curves from images are available within the SPOOK pipeline:

- The first one is extraction by using the software Astrometry24.net (A24N) by Sybilla Technologies [26], which is preferred whenever images contain enough stars to perform astrometric reduction and extract apparent magnitudes, provided that all the links of the pipeline work – i.e. A24N image processing, plus SPOOK's own tracklet linking and correlation;
- The second method uses AstroImageJ (AIJ) [6], and is applied when 1) the A24N solution fails or 2) the images do not contain enough stars for astrometric reduction (which actually triggers A24N failure) – this is the case e.g. when drastic windowing is used to increase frame rates.

5. LIGHT CURVE PREPROCESSING

This section focuses on each of the light curve processing steps that lead to the obtention of detrended light curves. These are:

1. atmospheric detrending,
2. range normalization and
3. polynomial fit.

The first step is only needed for instrumental light curves – i.e. A24N already gives apparent magnitudes, hence step 1 can be skipped when working with its output. The same is true for simulated light curves.

5.1. Removal of Atmospheric Effects

In the case of an instrumental light curve obtained by a ground observer, the measured magnitude is influenced by atmospheric attenuation, which generally depends on the airmass (amount of air in the line of sight) and the wavelength of the light. In SPOOK the following atmospheric attenuation model from [35] is used:

$$m_A - m_I = -k \cdot X + \mathrm{ZP} - t_f \cdot (\mathrm{CI})\,, \qquad (5)$$

where X is the airmass, ZP is the telescope *zero point* and CI is the colour index, which can be expressed e.g. in Blue minus Visible ($B-V$) or any of the other combinations of the Johnson-Cousins type of colour filters [4]. The parameters k and t_f are the slopes of the airmass and colour index effects, respectively.

Within SPOOK, k, ZP and t_f are calibrated with a linear least square regression against observations of known stars during the same night. Then, the model from Eq. 5 is used to convert the light curve to apparent magnitude.

Two options exist within SPOOK. The first is to calibrate with the Landolt standard stars [17], if the measurements are taken with any of the Johnson-Cousins filters. The second is to calibrate with the stars from the Gaia catalogue, specially those for which the effective temperature is well defined [2]; these are used to calibrate those measurements taken without any colour filter, so that the transmissivity curve is panchromatic over the near-visible light spectrum.

For the Gaia case, colour indices are not readily available, however. Nonetheless, the $B-V$ index is estimated from the effective temperature T_{eff} of each star, in K, as per Ballestero's formula [3]. Whatever the case, airmass is estimated from the zenith angle z of each star using Hardie's approximation [13].

5.2. Range Normalization

The second pre-processing step applied to instrumental light curves is range normalization. Apparent magnitude as calibrated with the aforementioned procedure measures the photon flux received at the telescope aperture as if there was no atmosphere. However, it still captures the changes in the distance relative to the observed object, a.k.a. range ρ, in the form of brightness variations. These are proportional to the inverse of the square of the range. Thus the magnitude calibrated as if the object was observed at a range of 1000 km can be obtained as

$$m_{A,1000} = m_A - 5\log_{10}\rho + 15\,, \qquad (6)$$

where ρ is in km. This process can also be applied directly to $m_I \rightarrow m_{I,1000}$ in case no atmospheric calibration is possible, to at least remove the effects of range.

5.3. Polynomial Fit

Having removed the influence of atmospheric attenuation and range from a light curve, there are still some other effects that can influence its moving average and envelope, such as time variations of the phase angle – e.g. for a Lambertian sphere, measured brightness decreases with higher phase angles, being the peak of maximum brightness at 0 phase angle. SPOOK has a final detrending step that computes a polynomial fit to the light curve and subtracts it. Typically, a 1- or 2-degree polynomial suffices, as the phase angle evolution itself from the point of view of a ground observer changes smoothly over time[2].

6. ATTITUDE CHARACTERIZATION

This section describes the SPOOK capabilities used to characterize the attitude of an object based on its light curve, without a-priori information on shape or reflectance properties. Two main attitude-related characteristics can be extracted with SPOOK:

1. Synodic rotation period: if the object rotates around itself at a stable angular velocity (i.e. around an axis close to a principal axis), the first relevant output is the dominant frequency or period of the light curve, which corresponds to the synodic period of the object.
2. Sidereal rotation period and axis: under certain observability conditions, it is possible to extract the sidereal period of rotation and spin axis – i.e. in an inertial frame.

6.1. Synodic Period

The first object characteristic that SPOOK can extract from its light curve is the synodic period. When a light curve has a marked periodical behaviour, the synodic period is the time that the repeated pattern lasts. This definition applies mainly to objects that rotate around one of their principal axes, hence producing light curves with one single fundamental frequency. With tumbling objects, which rotate around an axis that is not parallel to their angular momentum, two independent fundamental frequencies shall be observed instead, one corresponding to the rotation around a principal axis, and the other to the average period of precession around that axis [22]. Light curves from objects with non-periodical attitude behaviour (e.g. nadir-stabilized, actively controlled) will not present significant periodic behaviour either.

As the main spectral analysis tool to estimate synodic periods, SPOOK uses the generalized Lomb–Scargle (LS) periodogram [29], because of its adaptability to non-equispaced data[3] and its natural extensibility to accommodate more complex models.

The generalized LS is obtained by fitting a polynomial plus a Fourier series of the form

$$F_{n_p,n_h}(\mathbf{A},f,t) = \sum_{k=0}^{n_p} A_k t^k + \sum_{j=1}^{n_h} \left(A_{n_p+2j-1}\cos 2\pi j f t + A_{n_p+2j}\sin 2\pi j f t\right) \quad (7)$$

to the data. Here, $n_p \geq -1$ indicates the degree of the trend polynomial, while $n_h \geq 0$ indicates the number of harmonic terms of the Fourier series[4] with fundamental frequency f. $\mathbf{A} \in \mathbb{R}^m$ is the vector that stores the coefficients, with $m = 1 + n_p + 2n_h$. The generalized LS periodogram is equivalent to

$$P_{LS}(f) = \frac{1}{2}\left(\chi^2_{0,0} - \chi^2_{0,1}(\mathbf{A},f)\right), \quad (8)$$

where $\chi_{n_p,n_h}(f)$ is the weighted least squares (WLS) cost of the linear parameters to the data at each frequency,

$$\chi^2_{n_p,n_h}(\mathbf{A},f) = \sum_i \left(\frac{L_i - F_{n_p,n_h}(\mathbf{A},f,t_i)}{\sigma_i}\right)^2, \quad (9)$$

where $\mathbf{L} = \{L_i\} \in \mathbb{R}^n$ is the vector of n measurements (either flux or magnitude) at times $\{t_i\}$, with standard deviations $\{\sigma_i\}$, for all $i \in [1,n]$.

As indicated by [29], the LS periodogram can be further generalized with multiple polynomial and harmonic terms, by using $\chi^2_{n_p,n_h}$ with $n_p > 0$ and/or $n_h > 1$ instead of $\chi^2_{0,1}$ in Eq. 8. Incidentally, minimizing $\chi^2_{n_p,0}$ leads to the polynomial fit of the previous section.

Using the P_{LS} from Eq. 8, which is an approximation to he power spectral density of the signal, the synodic period can be identified as the inverse of the frequency that corresponds to the greatest common divisor of all the detected peaks in the periodogram. Alternatively, the more straight forward WLS approach can be used to calculate the periodogram with $n_h > 1$, so that the highest peak corresponds to the best fundamental frequency fit. Therefore, for principal axis rotators (e.g. spin-stabilized spacecraft), the LS periodogram can be used to obtain the synodic period of their light curve.

It is common that the detected fundamental frequencies correspond not to the total time by which the object performs a full revolution, but to an integer division of it,

[2] This might not be the case for a space observer.

[3] Note that some telescopes may not produce measurements at an exact constant frame rate, and light curves my have unavoidable arbitrary gaps due to e.g. a pier side change of the telescope mid-observation.

[4] When $n_p = -1$, the polynomial part is removed, while $n_h = 0$ eliminates the Fourier series part.

most commonly two [18]. This is due to the fact that objects with axial symmetry may repeat the same reflection pattern more than once in one full rotation – e.g. a cylinder rotating around an axis perpendicular to its length would produce a light curve whose pattern repeats exactly every half revolution.

Furthermore, with light curves whose average sample rates do not comply with the Nyquist criteria w.r.t. aliasing, the capability to estimate the correct synodic period becomes impaired. According to [29], it is still possible to uniquely extract the real fundamental frequency of a non-equispaced, under-sampled (in average) signal, despite aliasing. Nonetheless, in practice, for only weekly non-equispaced light-curves, aliasing still poses important difficulties.

Once a synodic period candidate T has been extracted from a light curve sampled at times t_i, in order to inspect it manually, SPOOK can generate its phase plot – it plots the light curve against its phase, defined as

$$p_i = \frac{t_i \mod T}{T} . \tag{10}$$

The most straightforward application of the phase plot is to visually inspect whether the periodic behaviour pattern has significant secondary harmonics or not, which can give a hint at whether the extracted period corresponds e.g. to a half rotation instead of a full one.

6.2. Sidereal Spin Axis and Period

The attitude of principal axis rotators can be defined with a rotation axis in inertial frame, represented by a unit vector or e.g. a pair of right ascension and declination angles, and a rotation rate or period. Within SPOOK, these parameters can be estimated from a light curve by means of the epoch method, adapted from the asteroid community [11, 12]. Hall et. al. applied the epoch method to recover the spin rate and axis of several space debris objects from their light curves. The main appeal of this method is that no a-priori knowledge about the shape or the reflective properties of the object is needed. Its main drawback, however, is that the attitude of tumbling objects cannot be characterized, and that it can only be used under specific observation conditions [12].

The epoch method is based on the assumption that the synodic period is the time it takes the phase angle bisector (PAB) to perform a full rotation around the object body, from the object point of view. The method then exploits this assumption to calculate the difference between the synodic period and the sidereal period – i.e. the time it takes the object to perform a full rotation around itself relative to the inertial frame. This difference becomes a function of the sidereal period itself, together with the direction of the spin axis. Thus, one can estimate the variations of the synodic period as measured using a sliding window along the light curve, and then fit these variations to the model of the synodic-sidereal period difference to estimate the sidereal spin axis and rate [11].

First, the Lomb–Scargle periodogram is computed on the whole light curve to estimate the average synodic period, as explained in the previous section. Then, a time window size is chosen to perform the time-varying estimation of the synodic period. Typical values are between 2 and 8 times the average synodic period. Shorter time windows lead to worse resolution on the period estimation, due to the wider peaks in the frequency domain, but are more sensitive to fast synodic period changes. Once the window size is chosen, SPOOK slides it along the light curve at $\{t_k\}$ time locations, for $k \in [1, n_T]$. At each evaluation time, it fits the best synodic period, together with the necessary polynomial and harmonic coefficients, to the model of Eq. 7, as per the weighted least squares regression of Eq. 9, as seen in the previous section. Thus, the n_T synodic periods $\mathbf{T} = \{T_k\}$ are estimated by minimizing $\chi^2_{n_p,n_h}(1/T_k)$ at each window. SPOOK solves this optimization problem with the *trust region* algorithm from [5], limiting the values of $\mathbf{T}$ to a small region around the estimated average synodic period.

Once the varying synodic periods $\{T_k\}$ have been obtained, SPOOK performs a non-linear WLS to fit the model of the synodic period over time as a function of the sidereal period of rotation T_S and the spin axis direction, which is represented as a right ascension and declination pair [11].

On the one hand, this method can only be used on light curves obtained in an observation scenario where the PAB changes significantly over time, but where the object itself has a sidereal rotation rate significantly faster (so that the core assumption is observed). On the other hand, due to the aliasing limitations of the Fourier-based sliding period search, the object needs to rotate slowly enough for its sidereal rotation rate to be significantly smaller than the average sample rate of of the light curve, which is conditioned by the exposure time needed for a good enough signal to noise ratio (SNR) and the readout time of the telescope. Therefore, the applicability of this method is constrained significantly by the observation geometry and the specifications of the sensor used.

7. RESULTS

7.1. Real Light Curves

This section demonstrates the preprocessing capability of SPOOK on an instrumental light curve from the morning of 2019-10-06, measured with ART and reduced with the AstroImageJ method. The light curve, shown in Figure 5, belongs to the ISO satellite with Cospar 1995-062A, which has a highly eccentric equatorial orbit, with perigee in LEO and apogee at twice the altitude of GEO. One of the images used to obtain this light curve is shown in Figure 4. The exposure time for the whole series of

images was 0.2 s, and every four pixels were binned into one. The ISO satellite is the dot at the centre of the triangle in the middle of the image. The rest of point features are stars, which do not appear as streaks due to the short exposure time and slow velocity of ISO in the component orthogonal to the telescope pointing.

In Figure 5, the faded blue squares correspond to the instrumental magnitude, while the red triangles are the apparent magnitude calibrated at a range of 1000 km. The black curve is the fit of a 2^{nd} order polynomial of time to the latter. The abscissa shows UTC time in $hh{:}mm$. The time step between observations is between 2.33 and 2.51 s, except for the gap in the middle.

Along the entire night, more than 12000 independent stars were observed and identified against the Gaia star catalogue from [2], spread along 220 different images properly reduced with A24N. All these stars were used to fit the model from Eq. 5 to the measured $m_A - m_I$ offset computed by A24N using a linear regression. Figure 6 shows the effective temperature distribution of these stars, which is used to obtain the $B - V$ colour index from Ballestero's equation [3]. Figure 7 shows the fitted trend for the night. In this figure, blue points are $(m_A - m_I)_{\text{measured}} + t_f \cdot (B - V)$ for each star observation, while the black line is the trend $-k \cdot X + \text{ZP}$. For this night, $k \simeq 0.2747$, ZP $\simeq 22.68$ and $t_f \simeq 0.4805$.

The instrumental light curve of ISO, shown in blue in Figure 5, has first been converted to apparent magnitudes by adding the right-hand side of Eq. 5 to the measured m_I, using the values of $k = 0.2747$ and ZP $= 22.68$ extracted from the aforementioned regression. The color index, however, is set to 0. The actual color index of ISO is not known and, in fact, it is most likely different for each of its surfaces due to varying reflexive properties; moreover, CI variations with time might be highly coupled with attitude itself, depending on the actual BRDFs of the surfaces of ISO. Therefore, ignoring these differences in CI might affect the power of the frequency harmonics on a Fourier-based analysis, but not their location in the frequency scale.

Second, the apparent magnitude has been normalized to 1000 km range, as per Eq. 6 (red triangles in Figure 5). Range and any other orbital parameters of the observed object are obtained with the orbit propagation capabilities of SPOOK [20, 23].

Figure 4. Image of the ISO satellite taken with ART.

The last step has been to subtract the parabolic trend, shown as a black curve in Figure 5, to the normalized apparent light curve. At this point, the data is indeed detrended from any other slowly varying effects such as the phase angle influence on brightness.

Next, a generalized LS periodogram with $n_p = 0, n_h = 1$ has been enough to detect the main periodic components of the light curve. As shown in Figure 8, the light curve contains one marked fundamental harmonic, followed by three secondary harmonics at twice, thrice and four times the fundamental frequency. No other significant power peaks above the noise floor are present, which indicates that most probably ISO is a principal axis rotator[5]. The fundamental harmonic peak falls at $f \simeq 29.85$ mHz, which corresponds to a synodic period of $T \simeq 33.51$ s.

Figure 9 shows the phase plot of the detrended light curve (blue triangles) using the synodic period of $T = 33.51$ s estimated from Figure 8. The black curve is the best fit of a $n_p = 0$, $n_h = 4$ Fourier series model to the data.

Unfortunately, this particular light curve was obtained when the object was midway between perigee and apogee, already moving at such a velocity that the PAB barely changed along the whole light curve. Therefore, no significant synodic period variation over time can be extracted from the light curve to motivate a search for the sidereal axis. On the other hand, because of this exact fact, the sidereal period of rotation of ISO at the epoch of this light curve was actually almost equal to the apparent one, so that $T_S \simeq T \simeq 33.51$ s.

7.2. Simulated Light Curves

This section reproduces again the SPOOK pipeline for attitude characterization from light curves, but for simulated data. Therefore, this section demonstrates the light curve simulation capability, and focuses especially on the sidereal spin axis and period determination part, which is not included in the previous case.

In this example, the simulated light curve originates from a cylinder, approximated as a prism with a 32-side regular polygon as base, of 10 m length and 1 m radius, which should be expected to produce light curves similar to those e.g. of a rocket body. Its surface only has diffuse Lambertian reflectance, with a non-homogeneous albedo distribution: one end of the prism absorbs all incoming light (albedo of 0.01), while the other reflects all (albedo of 0.99); the rest of the prism surface has an albedo of 0.13, except for a region close to the bright tip, where albedo is 0.43. This distribution was selected to emulate

[5] Although it could be that it actually has a tumbling motion whose main average precession frequencies share a greatest common divisor of comparable order of magnitude.

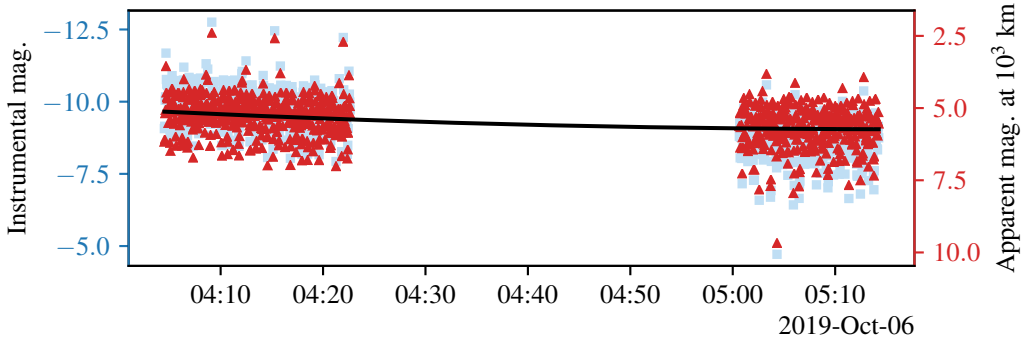

Figure 5. Light curve of the ISO satellite measured on the morning of 2019-10-06 with ART.

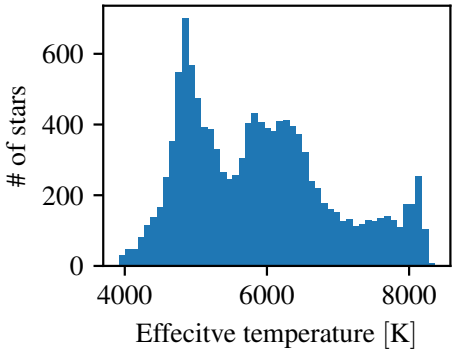

Figure 6. Histogram of the effective temperature distribution for the stars observed by ART on 2019-10-05/06.

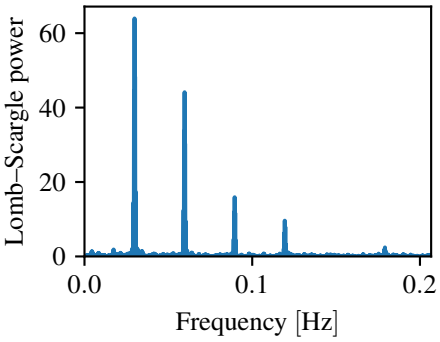

Figure 8. Lomb–Scargle periodogram the light curve from Figure 5, after detrending.

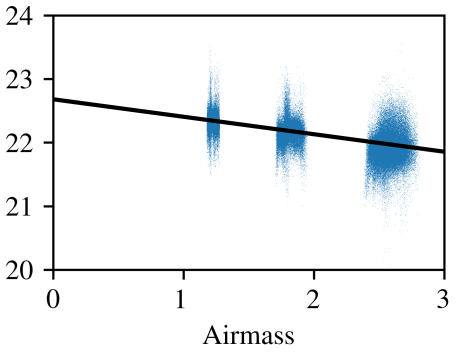

Figure 7. Apparent-instrumental magnitude offset as a function of airmass X for all the starts observed by ART on 2019-10-05/06.

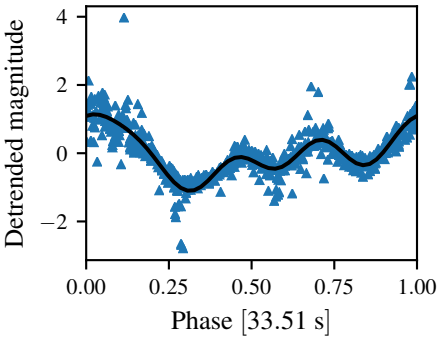

Figure 9. Phase plot of the detrended light curve from Figure 5.

a non-homogeneous albedo distribution, but it is otherwise arbitrary. Figure 11 shows a render of this shape, prodcuded with the open source tool FreeCad.

The object has a high eccentric orbit with 29183 km of semi-major axis, 94.9^{o} inclination, eccentricity of 0.76 and argument of perigee at 45^{o}, with the right ascension of the ascending node at 235^{o}. It has a stable rotation with a sidereal period of 115.86 s with a spin axis oriented at right ascension -90^{o} and declination -30^{o} in the inertial frame, and which is perpendicular to the longitudinal axis of the cylinder.

The simulation scenario consists in an observation from ART (6.63^{o}W, 38.22^{o}N) shortly after the midnight of 2021-01-01, for a span of about 40 minutes. The already range-detrended light curve is shown in Figure 10, where the blue triangles correspond to the apparent magnitude already calibrated at a range of 1000 km. The abscissa shows UTC time in $hh{:}mm$. The time step between observations is exactly of 5 s.

In this case, there is no lower-degree polynomial with time that fits the whole light curve nicely, so it has not been detrended further. Because of this, the Lomb–Scargle periodogram shows some residual power at very low frequency, but otherwise the extracted average synodic period is unaffected, as can be seen in Figure 12. The plot clearly shows a main peak at a fundamental frequency of $f \simeq 0.00874$ Hz, which corresponds to a synodic period of $T \simeq 114.4$ s. Two more minor harmonics of this frequency, at multiples 2 and 3 of the fundamental, can be observed, too. The high power around $f \to 0$ is due to the fact that the light curve has a slow trend that has not been removed.

The epoch method has been applied to this light curve, by sliding a window of four times the average synodic period (~ 458 s) at 5 s increments, and estimating the synodic period of each slice with a Fourier fit of $n_p = 1$, which compensates locally for not having fully detrended the light curve, and $n_h = 1$. Figure 13 shows the estimated synodic period. The blue triangles are the synodic period variation over time. The grey curve is the theoretical synodic period convolved with a rectangular window with ~ 458 s width, calculated from the known spin axis orientation and sidereal rotation period. The dashed black curve is the averaged synodic period, too, but calculated from the best fit spin axis orientation and sidereal rotation period, instead. Although it oscillates considerably around its theoretical value, the estimated synodic period displays no strong bias from the expected value. Therefore, even if the error of each individual synodic period estimation can be quite large, the overall time series of synodic periods can still be used to fit the synodic period model as a function of spin orientation and sidereal period.

The weighted least squares cost of this fit can be seen in Figure 14. The plot is in a Mollweide projection, where meridians are right ascension of the spin axis, while parallels are its declination. The colour scale is logarithmic. The white cross indicates the location of the known spin axis orientation (-90^{o}, -30^{o}), while the black *plus* sign indicates the best fit location (-89.4^{o}, -29.4^{o}) – it corresponds to a best fit sidereal period of 115.88 s, in contrast to the actual 115.86 s programmed in the simulation. Thus, the absolute minimum lies considerably close to the actual truth.

However, it is interesting to note that, with this particular light curve, a secondary region with very low cost exists around (43.98^{o}, 27.24^{o}) with a sidereal period of 115.66 s. This secondary solution corresponds to the spin configuration where the PAB in spin frame has an azimuthal movement roughly equal to that of the main solution, but with its z-component negated. A wider distribution of the PAB along the celestial sphere, with more drastic movements, if solvable, would prevent this secondary solution from appearing [25].

With this one and similar test cases, it has been seen that the epoch method tends to converge to the true solution better when fitting Fourier series with just one or, at most, two harmonics. With lower harmonic order, the synodic period presents a higher variance, as can be seen in Figure 13. When using higher order harmonics, the variance decreases, but a bias in the synodic period appears that displaces the optimal solution. Figure 15 shows a sliding synodic period calculated as in Figure 13, but using four harmonics instead of only one. In this particular simulation scenario, the bias may come from the fact that the amplitude of secondary harmonics seems to change along the light curve itself, which introduces an additional phase variation over time, other than the rate of change of the PAB – see how the shape of each period evolves with time in Figure 10. Conceivably, the higher order fit would capture these effects and displace the synodic period from its true value. Further analysis is needed to resolve this issue. Similar Biases were observed in [32].

Moreover, this method is highly sensitive to the size of the sliding window chosen to perform the synodic period calculation, and even a few outliers can add significant perturbations to the synodic period estimation. Therefore, to increase its confidence w.r.t. obtained results, the epoch method in a general case should be used on several light curves of the same object taken at different observation geometries [11, 25], or in conjunction with other methods such as shape-dependent attitude determination [12].

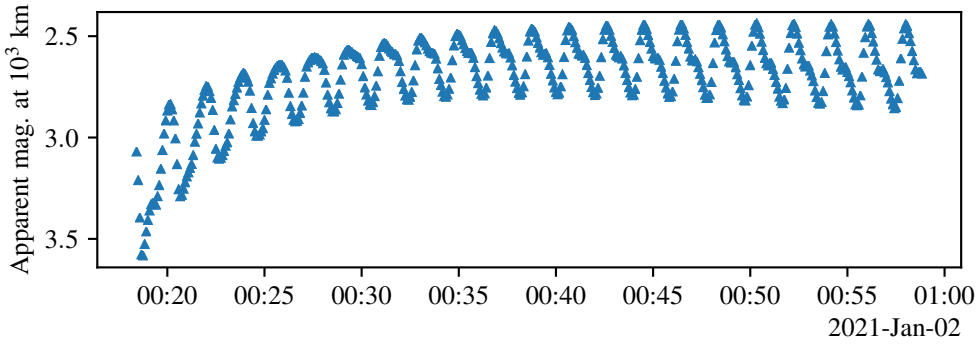

Figure 10. Light curve simulated with SPOOK, as observed by ART.

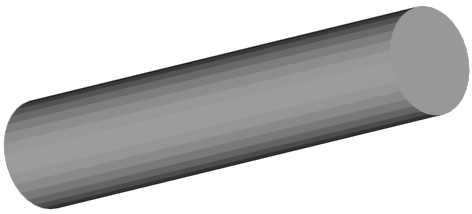

Figure 11. Render of a 32-base prism.

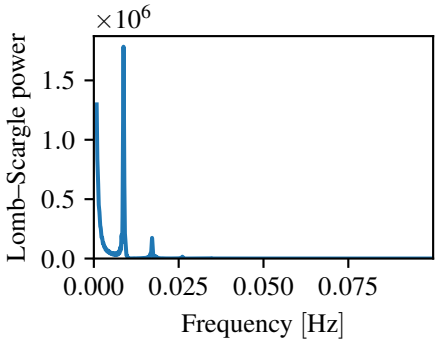

Figure 12. Lomb–Scargle periodogram of the light curve from Figure 10.

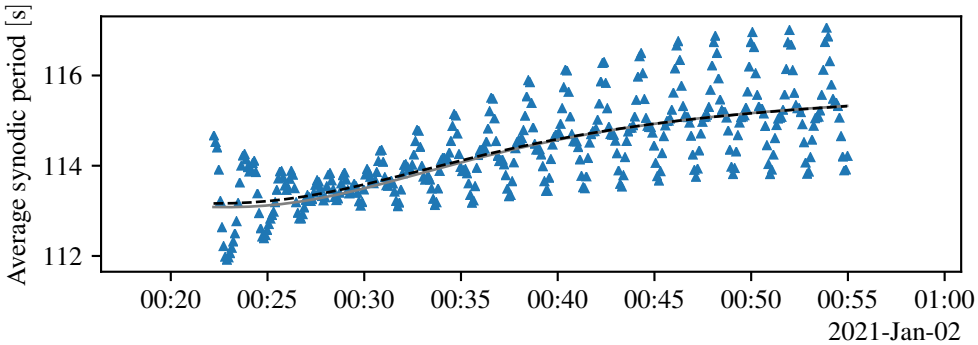

Figure 13. Sliding synodic period for the light curve from Figure 10.

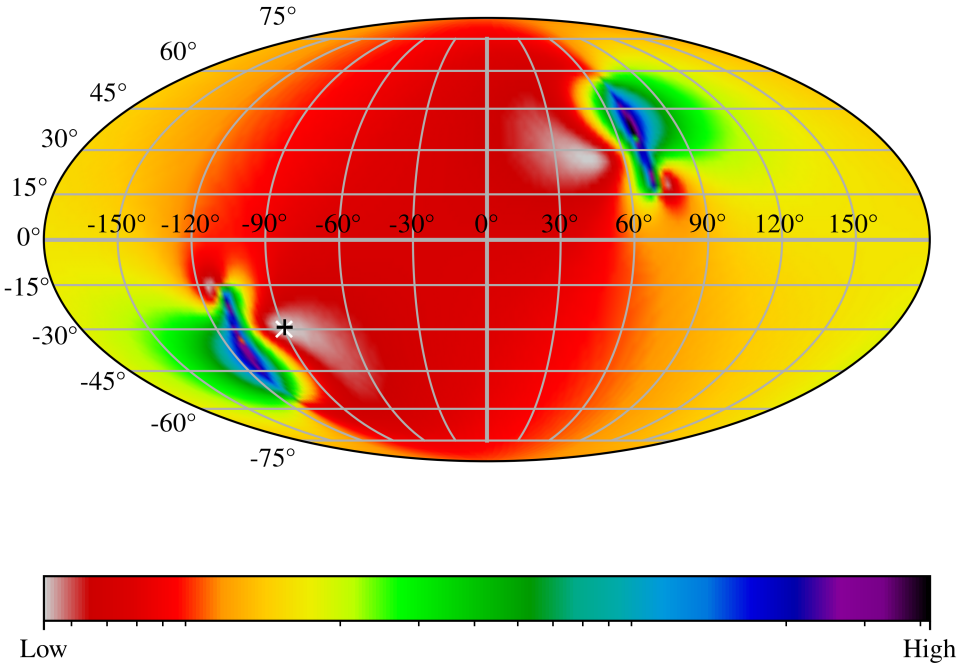

Figure 14. Weighted least squares cost of fitting the synodic period model.

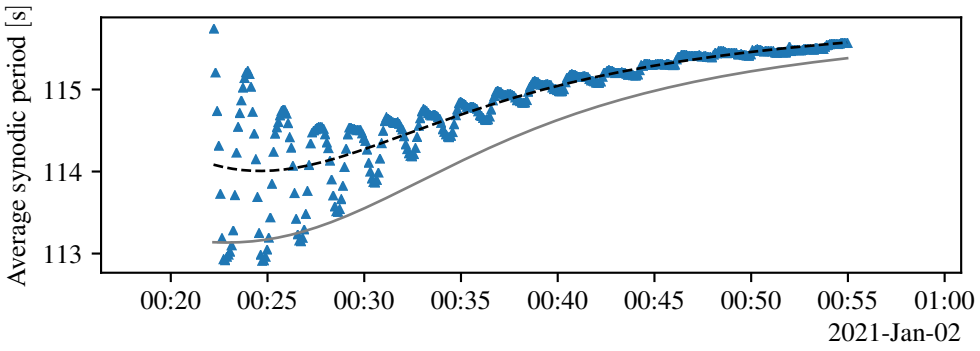

Figure 15. Sliding synodic period for the light curve from Figure 10, calculated using four harmonics.

8. CONCLUSION

New object characterization capabilities have been added to SPOOK, the SSA software framework of Airbus Defence and Space Germany, with the aim to enable an eventual systematic object characterization pipeline. New modules added are: light curve simulation, light curve extraction from images, light curve preprocessing and attitude characterization, consisting of synodic period and sidereal period/spin axis estimation. Synodic periods can be extracted from real light curves of stable rotators, and the epoch method implementation of SPOOK has been demonstrated against a simulated scenario, albeit some bias problems have been detected, in concordance with the literature on this method.

These new incorporations set the base, and provide the necessary tools, for a wider range of object characterization techniques to be incorporated within SPOOK.

ACKNOWLEDGMENTS

The first author of this paper would like to thank Jiři Šilha for his tips on light curve generation with AIJ.

REFERENCES

1. Ashikhmin M., Shirley P., (2001). An Anisotropic Phong BRDF Model, *Journal of Graphics Tools* **5**.

2. Bai Y., Liu J., Bai Z., et al., (2019). Machine-Learning Regression of Stellar Effective Temperatures in the Second Gaia Data Release, *The Astronomical Journal* **158**(2), 93. (Visited on 03/08/2021).

3. Ballesteros F. J., (2012). New Insights into Black Bodies, *Europhysics Letters* **97**(3), 34008. arXiv: 1201.1809.

4. Bessell M. S., (2005). Standard Photometric Systems, *Annual Review of Astronomy and Astrophysics* **43**, 293–336.

5. Byrd R. H., Schnabel R. B., Shultz G. A., (1988). Approximate Solution of the Trust Region Problem by Minimization over Two-Dimensional Subspaces, *Mathematical Programming* **40**(1), 247–263.

6. Collins K. A., Kielkopf J. F., Stassun K. G., et al., (2017). Astroimagej: Image Processing and Photometric Extraction for Ultra-Precise Astronomical Light Curves, *The Astronomical Journal* **153**(2), 77. (Visited on 01/15/2020).

7. Cook R., Torrance K., (1982). A Reflectance Model for Computer Graphics, *ACM Trans. Graph.* **1**, 7–24.

8. Du X., Wang Y., Hu H., et al., (2018). The Attitude Inversion Method of Geostationary Satellites Based on Unscented Particle Filter, *Advances in Space Research* **61**(8), 1984–1996.

9. *ESA's Annual Space Environment Report* (2020). GEN-DB-LOG-00288-OPS-SD. ESA Space Debris Office.

10. Furfaro R., Linares R., Reddy V., (2019). Shape Identification of Space Objects via Light Curve Inversion Using Deep Learning, in *Advanced Maui Optical and Space Surveillance Technologies Conference*.

11. Hall D., Africano J., Archambeault D., et al., (2006). AMOS Observations of NASA's IMAGE Satellite, in *Advanced Maui Optical and Space Surveillance Technologies Conference*.

12. Hall D., Kervin P., (2014). Optical Characterization of Deep-Space Object Rotation States, in *Advanced Maui Optical and Space Surveillance Technologies Conference*.

13. Hiltner W. A., (1962). *Astronomical Techniques*. Chicago: University of Chicago Press.

14. Holzinger M. J., Alfriend K. T., Wetterer C. J., et al., (2014). Photometric Attitude Estimation for Agile Space Objects with Shape Uncertainty, *Journal of Guidance, Control, and Dynamics* **37**(3), 921–932.

15. Kaasalainen M., Torppa J., (2001). Optimization Methods for Asteroid Lightcurve Inversion. I. Shape Determination, *Icarus* **153**(1), 24–36.

16. Kaasalainen M., Torppa J., Muinonen K., (2001). Optimization Methods for Asteroid Lightcurve Inversion. II. The Complete Inverse Problem, *Icarus* **153**(1), 37–51.

17. Landolt A. U., (2009). UBVRI Photometric Standard Stars Around the Celestial Equator: Updates and Additions, *The Astronomical Journal* **137**(5), 4186–4269. (Visited on 03/09/2020).

18. Linder E., Silha J., Schildknecht T., et al., (2015). Extraction of Spin Periods of Space Debris from Optical Light Curves, in *66th Astronautical Congress International*. Curran Associates, Inc.

19. Nicodemus F. E., (1965). Directional Reflectance and Emissivity of an Opaque Surface, *Applied Optics* **4**(7), 767–775.

20. Pedone G., Vallverdu Cabrera D., Dimitrova Vesselinova M. G., et al., (2021). SPOOK: A Tool for Space Objects Catalogue Creation and Maintenance Supporting Space Safety and Sustainability, in *7th Annual Space Traffic Management Conference*.

21. Piergentili F., Santoni F., Seitzer P., (2017). Attitude Determination of Orbiting Objects from Lightcurve Measurements, *IEEE Transactions on Aerospace and Electronic Systems* **53**(1), 81–90.

22. Pravec P., Harris A. W., Scheirich P., et al., (2005). Tumbling Asteroids, *Icarus*. Hapke Symposium **173**(1), 108–131.

23. Rodriguez Fernandez O., Utzmann J., Hugentobler U., (2017). SPOOK - A Comprehensive Space Surveillance and Tracking Analysis Tool, in *7th European Conference for Aeronautics and Aerospace Sciences*.

24. Rodriguez Fernandez O., Utzmann J., Hugentobler U., (2019). Correlation of Optical Observations to Catalogued Objects using Multiple Hypothesis Filters, in 1st NEO and Debris Detection Conference.

25. Somers P., (2011). Cylindrical RSO Signatures, Spin Axis Orientation and Rotation Period Determination, in *Advanced Maui Optical and Space Surveillance Technologies Cenference*.

26. Sybilska A., Kozłowski S., Sybilski P., et al., (2019). Astrometry24.Net – Precise Astrometry for SST and NEO, in 1st NEO and Debris Detection Conference. (Visited on 03/29/2021).

27. Torppa J., Muinonen K., (2005). Statistical Inversion of Gaia Photometry for Asteroid Spins and Shapes, in *The Three-Dimensional Universe with Gaia*. Ed. by C. Turon, K. S. O'Flaherty, M. A. C. Perryman. Vol. 576. ESA Special Publication.

28. Utzmann J., Dimitrova Vesselinova M. G., Rodriguez Fernandez O., (2019). Airbus Robotic Telescope, in 1st NEO and Debris Detection Conference.

29. VanderPlas J. T., (2018). Understanding the Lomb–Scargle Periodogram, *The Astrophysical Journal Supplement Series* **236**(1). arXiv: 1703.09824.

30. Vatti B. R., (1992). A Generic Solution to Polygon Clipping, *Communications of the ACM* **35**(7), 56–63.

31. Virgili B. B., (2016). DELTA Debris Environment Long-Term Analysis, in *Proceedings of the 6th International Conference on Astrodynamics Tools and Techniques*.

32. Wallace B., Somers P., Scott R., (2010). Determination of Spin Axis Orientation of Geosynchronous Objects Using Space-Based Sensors: An Initial Feasibility Investigation, in *Advanced Maui Optical and Space Surveillance Technologies Conference*. Ed. by S. Ryan.

33. Wetterer C. J., Linares R., Crassidis J. L., et al., (2014). Refining Space Object Radiation Pressure Modeling with Bidirectional Reflectance Distribution Functions, *Journal of Guidance, Control, and Dynamics* **37**(1), 185–196.

34. Williams V., (1979). Location of the Rotation Axis of a Tumbling Cylindrical Earth Satellite by Using Visual Observations, *Planetary and Space Science* **27**(6), 885–890.

35. Zigo M., Silha J., Krajcovic S., (2019). BVRI Photometry of Space Debris Objects at the Astronomical and Geophysical Observatory in Modra, in *Advanced Maui Optical and Space Surveillance Technologies Cenference*.